RSC Sustainability

ROYAL SOCIETY OF CHEMISTRY

PAPER

View Article Online
View Journal

Cite this: DOI: 10.1039/d5su00830a

Low-temperature transformation of mechanochemically treated oyster shells into nanocrystalline apatites

Carla Triunfo, [a] Francesca Oltolina, [b] Annarita D'Urso, [b] Raquel Fernández-Penas, [c] Giuseppe Falini, [a] Antonia Follenzi [b] and Jaime Gómez-Morales *[c]

A technique combining an extended mechanochemical treatment of biogenic calcium carbonate (bCC) with a one-pot hydrothermal method was used for the first time to prepare nanocrystalline apatite. When calcitic bCC from oyster shell waste was subjected to dry milling for 1 hour (DM) the crystallite size of calcite was decreased from 92 to 14 nm, and the minimum temperature to achieve the complete conversion to apatite (T_{min}) decreased from 160 °C to 80 °C. In contrast, wet milling (18 h) induced polymorphism and amorphization, yielding calcite, aragonite, and amorphous calcium carbonate, with crystallite sizes of 7 nm for calcite and 13.7 nm for aragonite. The T_{min} decreased from 160 °C to 40 °C. Both transformations occurred *via* brushite as an intermediate metastable phase. Kinetic experiments evidenced that DM-bCC transformed faster than WM-bCC at T_{min}, achieving 98% *versus* 82% after 4 days, even though the complete transformation took 7 days. Both bCCs and the derived Ap nanoparticles demonstrated cytocompatibility with MS1 endothelial cells and m17.1 ASC murine mesenchymal stem cells. This synthetic approach offers a cost-effective, eco-friendly (without releasing CO_2), sustainable, and scalable (by using already established glass reactor technology rather than costly autoclaves) solution for valorising shells waste.

Received 29th October 2025
Accepted 6th December 2025

DOI: 10.1039/d5su00830a

rsc.li/rscsus

Sustainability spotlight

Mollusk shells, composed of biogenic calcium carbonate, represent a significant waste by-product from marine aquaculture, canning industries, and seafood restaurants. Currently, this waste is often disposed of in the ocean or landfills, resulting in unpleasant odors and health concerns. A technology that couples a mechanochemical treatment with a one-pot precipitation method transforms this waste into valuable apatite nanoparticles for biomedical uses at relatively low temperatures. The technology is low-cost, eco-friendly (avoids the release of CO_2), and scalable using glass reactor technology. Importantly, this approach aligns with the UN's Sustainable Development Goal 12 on responsible consumption and production, and contributes to targets 12.4, by eliminating landfill waste and CO_2 emissions, and 12.5, by facilitating the recycling of shells.

1. Introduction

The demand for biocompatible materials in the medical and dental fields has increased significantly, leading to a growing need for calcium phosphate apatites (Ap) to produce apatite-based products such as implants, coatings, and fillers. In 2024, the global apatites market was valued at approximately USD 2.54 billion and is expected to grow at a CAGR of 7.5% between 2025 and 2030.[1] The search for new calcium sources and low-cost sustainable precipitation methods to produce Ap in the last decade has focused on the use of natural resources that are considered a waste in different economic sectors, with focus on the promotion of the circular economy. Different biogenic $CaCO_3$ (bCC) biominerals have been used as a source of calcium to produce Ap including eggshells,[2] mussel shells,[3] clam shells,[4] cockle shells,[5] oyster shells,[6] snail shells,[7] corals[8] and cuttlefish bones.[9] Mollusk shells represent a waste by-product from marine aquaculture, canning industries and seafood restaurants. The shells constitute between 65 and 90% of the live weight of mollusks, depending on the species.[10] They are made up of calcium carbonate ($CaCO_3$) and an organic matrix (OM) primarily composed of proteins and polysaccharides. Currently, this waste is disposed of in the ocean or in landfills, leading to unpleasant odors and health concerns due to microbial decomposition.[11–13] Existing disposal methods, such as incineration or burial, pose environmental and economic challenges and result in the loss of valuable biomaterials.[14] Repurposing these residues into new materials, as

[a]Department of Chemistry "Giacomo Ciamician", University of Bologna, via P. Gobetti 85, 40129 Bologna, Italy
[b]Dipartimento di Scienze della Salute, Università del Piemonte Orientale, "A. Avogadro" Via Solaroli 17, 28100 Novara, Italy
[c]Laboratorio de Estudios Cristalográficos, IACT-CSIC, Avda. Las Palmeras 4, 18100 Armilla, Spain. E-mail: jaime.gomez@csic.es

apatite nanoparticles (Ap NPs), could help address these issues, providing an opportunity for shell valorization and stimulating the circular blue bioeconomy.[15] Among methods used to prepare Ap NPs from $CaCO_3$ biominerals, some approaches based on calcination-titration, mechanosynthesis and hydrothermal treatment have been recently reported.[16] Calcination-titration methods involve two main steps: first, calcining $CaCO_3$ at 900–1200 °C to produce CaO and CO_2, followed by an acid–base reaction of H_3PO_4 (or an acidic P reagent) with hydrated CaO.[3,17–19] A multistep method involved calcination followed of carbonation of the resulting CaO to produce precipitated $CaCO_3$, and then reaction with $(NH_4)_2HPO_4$ at 160 °C to yield Ap NPs.[20] The calcination-based methods fully destroy the intracrystalline OM and are unsustainable due to high temperature requirements and significant CO_2 emissions (about 44 g CO_2 per mol $CaCO_3$). Mechanosynthesis is a one-step process that uses mechanical energy to induce chemical reactions. This energy can cause defects, reduce particle size, and even induce amorphization into the materials, significantly enhancing their chemical reactivity and leading to solid-phase transformations.[21] Examples of materials produced by mechanosynthesis include nanoparticles of metal oxides,[22] cadmium sulphide (CdS),[23] $CaCO_3$ [24] and Ap.[25] The use of bCC to produce Ap NPs by mechanosynthesis is relatively recent. P reagents commonly used in this process include $(NH_4)_2HPO_4$ or H_3PO_4.[26–28] After mechanosynthesis, an additional drying step was necessary to completely transform $CaCO_3$ to Ap NPs. The drying process was carried out at 120 °C when using cuttlefish bone (aragonite) and 150 °C for eggshells or mussel shells, which are primarily composed of calcite or a combination of calcite and aragonite, respectively.[26,27] Furthermore, a method that combines the calcination of $CaCO_3$ with the mechanosynthesis of the resulting CaO with H_3PO_4 has also been reported to obtain Ap NPs.[4]

The hydrothermal method, by definition, involves the use of high temperatures (≥ boiling point) and pressures ≥ 1 atm. A study reported that hydrothermal synthesis transformed oyster shells bCC into Ap NPs in the presence of KH_2PO_4 or $(NH_4)_2HPO_4$ using Ca/P ratio 1.67. This process was conducted at 200 °C in a Teflon-lined stainless-steel autoclave. However, the transformation was found to be incomplete after 4 days reaction.[29] Recently, our group has set up a hydrothermal method to fully transform bCC from oyster shells of the species *Crassostrea gigas* into osteoinductive Ap NPs at $T \leq 160$ °C.[30] The technique employs KH_2PO_4 or K_2HPO_4 and bCC at different Ca/P ratios, in experiments lasting for 7 days. The bCC was obtained after 2 min dry-milling of the shell and sieved at $Ø = 45$ μm. The hydrothermal approach is one-step, straightforward, avoids the use of strong acids, and, importantly, prevents the emission of CO_2 to the atmosphere. Later on, the method was employed to synthesize M^{2+} doped Ap NPs ($M^{2+} = Mg^{2+}$, Mn^{2+}, Co^{2+}).[31] To scale the method to an industrial level using current glass crystallizer technology, thereby avoiding the need for expensive autoclaves and lowering the energy consumption, the T_{min} should be decreased significantly. We hypothesize that since the conversion proceeded *via* a dissolution-precipitation mechanism,[30] this goal could be achieved by reducing the bCC crystallite size through extended mechanochemical treatments. Previous reports have indicated that ball milling reduces particle size, induces amorphization, introduces lattice defects, and enhances the solubility of $CaCO_3$ in water.[32,33] In this study, we present the results of combining either a dry-milled (1 h) or wet-milled (18 h) treatment of the bCC with the one-pot transformation at temperatures ≤ 80 °C to produce Ap NPs. Furthermore, we have evaluated the morphological and electrokinetic properties of the resulting NPs in physiological conditions, as well as their cytotoxicity on two different cell lines, to determine if they are suitable for use in biomedicine.

2. Experimental

2.1. Preparation of starting $CaCO_3$ materials

Crassostrea gigas oyster shells (supplied by F. Terzi, Palosco, BG, Italy) were firstly washed with tap water. They were then immersed in a 5 wt% NaClO solution for 24 hours. After the treatment, the shells were rinsed with deionized water, dried, and subsequently ground using a hammer mill. The resulting material was then sieved through a mesh with a pore diameter of $Ø = 45$ μm. The biogenic $CaCO_3$ grains obtained in this manner are referred to as bCC (the reference material). Following this, the bCC particles were dry milled (DM) using 100 g ZrO_2 balls in a 500 mL ZrO_2 jar. This milling process was carried out in a planetary ball mill (PM 100 by Retsch) at a speed of 400 rpm for 1 hour. After milling, the material was sieved using a mesh with a pore diameter of $Ø = 45$ μm, resulting in a product designated as DM-bCC. Subsequently, the DM-bCC sample underwent a treatment of wet milling (WM). This procedure involved mixing 1.8 g of the dry-milled powder with 100 g of ZrO_2 balls, 200 mL of cyclohexane, and 0.2 grams of Na_2CO_3 in a ZrO_2 jar. Cyclohexane was used as a milling solvent since it produced the higher amorphization degree of bCC among ethanol, isopropanol, cyclohexane, heptane, and butanol in a previous study.[33] The mixture was subjected to grinding in a planetary ball mill for a duration of 18 hours, employing grinding cycles consisting of 10 minutes of grinding at 400 rpm followed by 20 minutes rest periods. The final product obtained from this treatment is referred to as WM-bCC. Following the wet milling process, cyclohexane was fully recovered using a rotary evaporator and subsequently reused in further milling cycles, contributing to the overall greenness and sustainability of the process. Cyclohexane and Na_2CO_3 (ACS reagent, ≥99%) were purchased to Sigma Aldrich.

2.2. Conversion of starting $CaCO_3$ materials to calcium phosphate

The experiments were conducted using 10 mL glass Pyrex tubes equipped with PBT screw caps and a rubber disc coated with PTFE. The tubes were filled to 70% volume with aqueous suspensions containing 300 mM KH_2PO_4 and either DM-bCC or WM-bCC, maintaining a P/Ca ratio of 0.6 (stoichiometric), without adjusting the pH. The samples were then subjected to temperatures in the range 25 °C ≤ T ≤ 100 °C, with increments of 20 °C, in an oven with circulating forced air for a duration of 7

days. After identifying T_{min}, the kinetics of the transformation at this temperature was studied in the time interval from 6 h to 7 days. The final suspensions were washed with deionized water by using a centrifuge (3 cycles) and then freeze-dried at −50 °C under vacuum (3 mbar) for 12 h. KH_2PO_4 (ACS reagent, ≥99% purity) was purchased to Sigma-Aldrich. All solutions were prepared with deionized water (0.22 mS, 25 °C, Milli-Q, Millipore).

2.3. Powder characterization

X-ray powder diffraction (XRD) patterns were acquired with a Bruker D8 Advance Vario Series II powder diffractometer (Bruker AXS, Bruker GmbH, Karlsruhe, Germany) equipped with $CuK_{\alpha 1}$ radiation (1.5406 Å) generator. Quantitative phase composition analysis of the obtained samples was performed using the Rietveld method with TOPAS 7.0 software (Bruker AXS, Bruker GmbH, Karlsruhe, Germany). This software was also employed to determine the crystallite size of the new samples, performing the full peak profile fitting of the XRD pattern. Fourier Transform Infrared Spectra (FTIR) were recorded in transmittance mode with a Hyperion 3000 (Bruker, Massachusetts, USA) instrument in the wavenumber range from 4000 cm^{-1} to 400 cm^{-1}. The instrument was equipped with an attenuated total reflectance (ATR) accessory of diamond crystal. Raman spectra were recorded with a LabRAMHR spectrometer (Jobin-Yvon, Horiba, Tokyo, Japan) equipped with a laser diode emitting at a wavelength of 532 nm. Crystal size distribution (CSD) was analysed by dynamic light scattering (DLS) with a Malvern Zetasizer Nano ZS analyzer (Malvern Instruments Ltd, Malvern, UK). The analysis was conducted on aqueous suspensions (~0.5 mg mL^{-1}, RT) contained in disposable polystyrene vials. For ζ-potential *versus* pH measurements, the pH of the suspensions was adjusted using 0.25 M HCl and 0.1 M NaOH solutions as titration agents, without adding any additional electrolytes. Transmission electron microscopy (TEM) was conducted with a Libra 120 Plus TEM instrument (EELS, Carl Zeiss, Jena, Germany) at an acceleration voltage of 80 kV. Samples were dispersed in absolute ethanol (99.8% v/v) and deposited on copper microgrids coated with a FORMVAR carbon film before observation. High-resolution TEM (HRTEM) analysis was performed with a TITAN G2 60-300 FEI Instrument (FEI, Hillsboro, OR, USA) operating at 300 kV. The instrument is equipped with EDX Super X detector to perform microanalysis and STEM type HAADF. For field emission scanning electron microscopy (FESEM) observations, we used a GEMINI LEO 1500 (Zeiss, Jena, Germany) instrument provided with an energy dispersive X-ray spectroscopy (EDX) analyzer by Oxford Instruments.

2.4. Cell lines and culture conditions

Murine pancreatic endothelial MS1 cells (ATCC CRL-2279™) were cultured in Dulbecco's Modified Eagle's Medium (DMEM; Sigma-Aldrich, St. Louis, MO, USA) enriched with 10% foetal bovine serum (FBS), 2 mM L-glutamine, and an antibiotic mix containing streptomycin (100 μg mL^{-1}) and penicillin (100 U mL^{-1}). The m17.ASC cell line, a clone of immortalized mesenchymal stem cells derived from mouse subcutaneous adipose tissue,[34] was maintained in Claycomb medium (Sigma-Aldrich), similarly as described above. Both cell types were incubated under standard conditions (37 °C, 5% CO_2).

2.5. Cytotoxicity tests

To determine the cytotoxicity of the NPs, MS-1 and m17.ASC cells were seeded at densities of 6000 and 5000 cells per well, respectively, into 96-well plates and cultured for 24 hours. Samples at concentrations ranging from 0.1 to 100 μg mL^{-1} were added in 100 μL of fresh medium. After a 72 hours incubation period, cell viability was assessed using a colorimetric assay based on 3-(4,5-dimethylthiazol-2-yl)-2,5-diphenyl tetrazolium bromide (MTT; Sigma-Aldrich, St. Louis, MO, USA). MTT solution (20 μL of 5 mg mL^{-1} in PBS) was added to each well and incubated for 2 hours at 37 °C. Supernatants were removed, and 125 μL of 0.2 N HCl in 2-propanol was added to solubilize the resulting formazan crystals. A volume of 100 μL from each well was transferred to a fresh 96-well plate, and absorbance was measured at 570 nm using a Victor™ X4 Multilabel Reader (2030; PerkinElmer, Shelton, CT, USA). Cell viability was expressed as a percentage relative to untreated controls, which were set at 100%. Each experimental condition was tested in triplicate, with a minimum of three independent experiments conducted to ensure reproducibility.

Statistical analysis. The statistical analysis was carried out using GraphPad Prism version 10.2.3 for Windows, developed by GraphPad Software (GraphPad Prism, San Diego, CA, USA). The results were presented using a one-way ANOVA with the relevant post-test for grouped analyses, and the mean ± standard deviation of at least three triplicates. Differences with values of $p < 0.05$ (*), $p < 0.01$ (**), $p < 0.001$ (***), and $p < 0.0001$ (****) were considered statistically significant.

3. Results and discussion

3.1. Influence of mechanochemical treatment of bCC on T_{min}

Fig. 1a shows XRD patterns of the oyster shell powder bCC (1-2 min milling, the reference material), DM-bCC (1 h milling) and WM-bCC (17 h treatment). In it, bCC and DM-bCC present the characteristic XRD patterns of calcite (PDF 05-0586), whose main reflection is at $2\theta = 29.3°$ (104). The widening of the reflections of the DM-bCC compared to bCC reflects the decrease in the crystallite size of the particles from 92 to 14 nm.

The WM-bCC sample, on the other hand, exhibits the most intense reflections of calcite at 2θ 29.3° (104) and aragonite at 26.1° (111) (PDF 41-1475) along to other weaker reflections of both phases, and the presence of amorphous calcium carbonate (ACC) as deduced by the bulging of the baseline. The composition of this sample was 45 wt% calcite, 26 wt% aragonite and 28 wt% ACC. The crystalline domain sizes of calcite and aragonite were, respectively, 7 and 13.7 nm. The occurrence of multiple phases suggests that calcite undergoes a dissolution or melting process, potentially facilitated by the presence of Na_2CO_3, followed by reprecipitation.[33] In addition, the use of

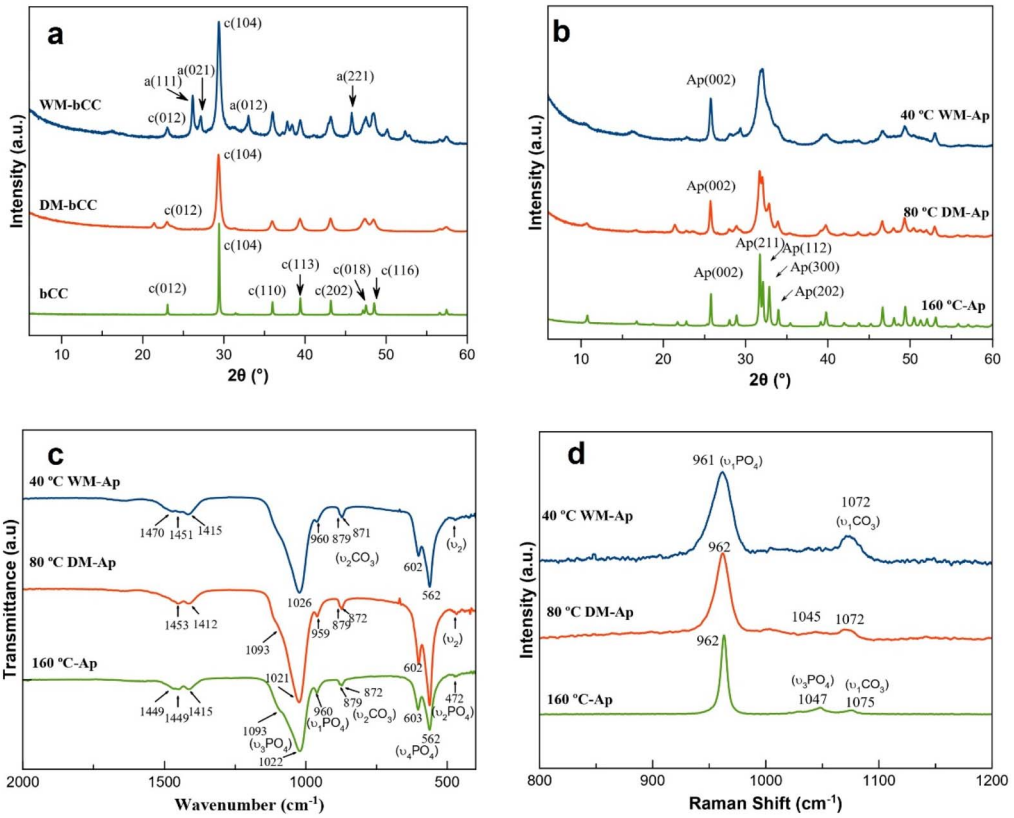

Fig. 1 (a) XRD patterns of starting $CaCO_3$ materials including bCC, DM-bCC and WM-bCC. The diffraction patterns are presented using different intensity scales to ensure that all diffraction peaks are clearly visible. (b)–(d) Characterization of Ap samples obtained by one-pot transformation of the starting $CaCO_3$ materials at the T_{min} which are labelled in the figures. (b) XRD patterns; (c) FTIR spectra, and (d) Raman spectra. In panels (a) and (b), the primary reflections of apatite and calcite, denoted as Ap and c, respectively, are followed by their corresponding Miller indices.

cyclohexane as milling solvent produced a higher degree of amorphization of the bCC as previously reported.[33] When transforming bCC to Ap in experiments lasting 7 days (Fig. 1b and S1), the T_{min} was found to be 160 °C. However, for the DM-bCC and WM-bCC samples, the T_{min} decreased significantly to 80 °C and 40 °C, respectively. Along with the decrease in T_{min}, the XRD peaks widened, indicating a progressive nanocrystalline character of the Ap. The crystalline domain sizes were measured to be 152 nm for Ap obtained from bCC (referred to as 160 °C-Ap-blank), 20 nm for Ap derived from DM-bCC (sample 80 °C DM-Ap), and 12 nm for Ap obtained from WM-bCC (sample 40 °C WM-Ap). Regarding the evolution of the transformation of bCC to Ap with the temperature, for the DM-bCC (Fig. S1a) at 25 °C, some of the calcite was transformed to brushite ($CaHPO_4 \cdot 2H_2O$), and then in the interval from 30 °C to 40 °C, to Ap, with decreased presence of brushite. At 60 °C, the brushite disappeared, but a small remnant of the calcite phase, represented by the reflection at 29.3°, still persists. This reflection disappeared at 80 °C. The main reflections of brushite were found at $2\theta = 11.5°$ (002), 20.8° (−121), and 29.2° (−141) [PDF 01-0395], while those of Ap were observed at 25.8° (002), 31.65° (211), 32.05° (112), 32.7° (300) and 33.9° (202) [PDF 01-1008]. For the WM-bCC (Fig. S1b), however, we obtained brushite plus Ap at 25 °C, and only Ap at 40 °C, with less than 1 wt% calcite. It was shown that the transformation of $CaCO_3$ to Ap takes place *via* a dissolution-precipitation mechanism driven by the favorable balance between Ap precipitation and $CaCO_3$ dissolution, due to the lower solubility product of hydroxyapatite than that of $CaCO_3$ (calcite or aragonite) at all the tested temperatures.[30] The significant reduction of T_{min} from 160 °C to 80 °C when using the DM-bCC sample must be ascribed to the enhanced reactivity caused by reduction of the crystallite size. In the case of WM-bCC sample, besides a reduction of crystallite size, the presence of aragonite and ACC, with a higher solubility than calcite favors the transformation, thereby reducing consistently the T_{min}. FTIR spectra of the obtained Ap samples in the wavelength range 400–2000 cm^{-1} (Fig. 1c) display the asymmetric stretching $\nu_3(PO_4)$ at 1000–1100 cm^{-1}, symmetric stretching $\nu_1(PO_4)$ at 960 cm^{-1}, the bending mode $\nu_4(PO_4)$ at 562 cm^{-1} and 603 cm^{-1}, and the $\nu_2(PO_4)$ mode at 472 cm^{-1}. In the Raman spectra (Fig. 1d), the main vibration was at ~960 cm^{-1}, corresponding to $\nu_1(PO_4)$ of Ap, and at 1072–1075 cm^{-1}, due to the $\nu_1(CO_3^{2-})$ mode, while the small band at 1047 cm^{-1} corresponds to $\nu_3(PO_4)$. The widening of this band when decreasing the T_{min} reflects the progressive increasing nanocrystalline character of Ap particles, as observed in the XRD patterns. In the three FTIR spectra of Fig. 1c, the presence of the weak band around 875 cm^{-1} due to

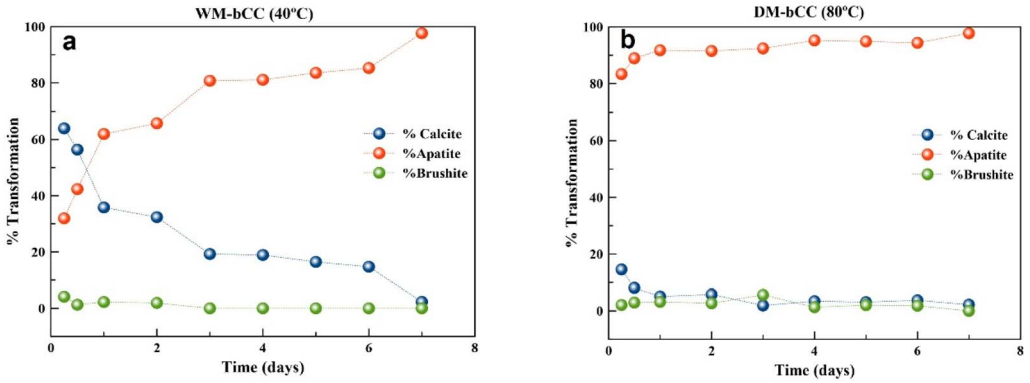

Fig. 2 Evolution of the mineral phase transformation of DM-bCC at 80 °C (a) and of WM-bCC at 40 °C (b) to Ap within the time interval between 6 h and 7 days. At time 0 h, the DM-bCC sample is composed of calcite, while the WM-bCC, labelled as $CaCO_3$ (tot) is a mixture of calcite, aragonite and ACC.

vibration mode $\nu_2(CO_3)$, is composed of two sub-bands at 879 and ~871 cm^{-1}, which are attributed to A-type (CO_3^{2-} replacing OH^-) and B-type (CO_3^{2-} replacing PO_4^{3-}) carbonate groups. Finally, the bands in the range 1415 to 1470 cm^{-1} are also ascribed to vibrational modes of CO_3^{2-}.[35]

3.2. Evolution of bCC conversion to apatite with time at T_{min}

It was observed that DM-bCC transformed more quickly than WM-bCC at shorter time intervals, achieving more than 98 wt% of Ap with only a negligible amount of brushite remaining after 4 days, and complete transformation was achieved after 7 days. In contrast, the conversion of WM-bCC was slower, yielding approximately 82% Ap after 4 days, while brushite disappeared after 3 days. Full conversion of WM-bCC also required 7 days (see Fig. 2 and S2).

Although both transformations proceed *via* an intermediate metastable phase (the brushite), the results indicate different conversion kinetics. This finding can be attributed to the influence of various factors: (i) polymorph composition and crystallite size, which affect the solubility and dissolution rates of DM-bCC and WM-bCC, and (ii) the different T_{min} at which Ap precipitates, which plays a key role on the nucleation kinetics of Ap, since it improves with increasing T.[36] This is due basically to the negative dependence of the solubility of the Ap on the temperature.[37,38] It is thus shown that the bCC mechanochemical treatments have a great impact on T_{min}, which supports the proposed hypothesis based on the reduction in crystallite size of the bCC samples. Furthermore, the induced polymorphism in the WM-bCC sample (composed of calcite, aragonite and ACC) can have contributed to decreasing T_{min} further compared to DM-bCC, thanks to the higher solubility of ACC and aragonite than that of calcite.[39] The above results suggest that to design a robust transformation process by the one-pot method, the choice between DM-bCC and WM-bCC is crucial, but it should be considered not only in terms of T_{min} and transformation kinetics, but also in relation to other factors, such as the purity of the samples, and the physicochemical and biological characteristics of the obtained Ap particles in relation to the projected biomedical applications.

3.3. Morphological, microstructural and electrokinetic properties of apatite particles

The morphological characterization by SEM revealed the presence of aggregates of calcite particles obtained after dry-milled

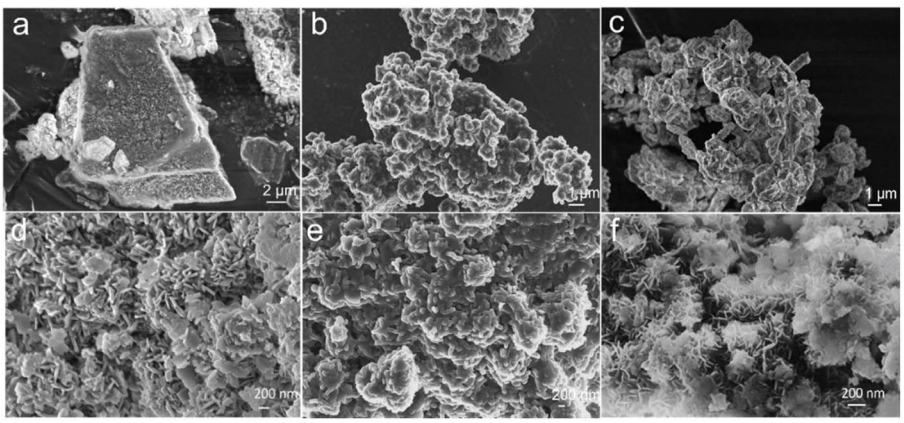

Fig. 3 Scanning electron micrographs of starting $CaCO_3$ crystals: (a) bCC, (b) DM-bCC, and (c) WM-bCC, and of the corresponding Ap crystals obtained *via* one-pot transformation after 7 days of the reaction: (d) 160 °C-Ap, (e) 80 °C-DM-Ap and (f) 40 °C-WM-Ap.

(Fig. 3b) and wet-milled (Fig. 3c) treatments of the bCC particles shown in Fig. 3a. The large unmilled bCC plaques were fully disassembled after the mechanochemical treatments, yielding the DM-bCC and WM-bCC samples. When transforming DM-bCC into the Ap sample at 80 °C (sample 80 °C-DM-Ap), we observe the formation of aggregates composed of elongated nanocrystals (Fig. 3e) with a (Ca + Mg)/P ratio of 1.79 ± 0.07 and an average length (L) of 47 ± 7 nm. In contrast, the 40 °C-WM-Ap sample displayed plate-like structures with a Ca/P ratio of 1.61 ± 0.03 and a length of 127 ± 34 nm, arranged in flower-like morphologies (Fig. 3f). Notably, no magnesium (Mg) was detected by EDX in the 40 °C-WM-Ap sample. This is likely due to the extended duration of the treatment and the use of the solvent. These morphologies are distinct from those observed in the sample 160 °C-Ap-blank, where the platelets have an average length of 45 ± 9 nm and a (Ca + Mg)/P ratio of 1.73 ± 0.03 (Fig. 3d). Mg^{2+} is an important trace element in biological apatite, present in bone, enamel, and dentin at characteristics weight percentages. Magnesium deficiency adversely affects all stages of skeletal metabolism, causing cessation of bone growth, decrease of osteoblastic and osteoclastic activities, osteopenia and increased bone fragility.[40,41]

Fig. 4 shows TEM images of the nanoplates composing the 80 °C-DM-Ap sample (Fig. 4a) and of the elongated nanocrystals of the 40 °C-WM-Ap sample (Fig. 4c and d). The corresponding SAED patterns (Fig. 4b) and (Fig. 4e) of these crystals display rings of the (002) and (121) planes (Fig. 4b) and (002), (121), and (300) planes (Fig. 4e) characteristics of the Ap phase. The HRTEM images of the 80 °C-DM-Ap sample (Fig. 4f and g) display lattice fringes whose d-spacings (0.81 nm) correspond to the crystallographic plane Ap (100). Additionally, Fig. 4h displays the HAADF-STEM image of this sample. Their EDX mappings of Ca and P (Fig. 4i), and Mg (Fig. 4j), reveal a homogeneous distribution of these elements within the crystals. Mg^{2+} was not supplemented to the mother solution. Still, it was present (5% atom) in the starting bCC, which had to be dissolved, thereby delivering Ca^{2+} and Mg^{2+} to the $H_2PO_4^-$ solution, before the Ap precipitation.

Importantly, the characterization of the CSD and electrokinetic properties, such as the ζ-potential as a function of pH, are essential for anticipating the future applications of the newly developed Ap NPs. These nanoparticles could serve as nanocarriers for luminescent dyes, chemotherapeutic, anti-inflammatory and antibiotic drugs, as well as for proteins and gene delivery.[42–48] Additionally, they could function as implantable osteoinductive materials for bone tissue engineering.[30,49] The stability of a colloidal suspension in simulated physiological environments, such as blood (pH ∼ 7.4) or in a tumour microenvironment at pH 6–7, depends on both the particle size and the surface charge of their particles. While maintaining colloidal stability is essential for nanoparticles used as nanocarriers,[50,51] it is not necessarily a decisive factor when these particles are used as a filler material. Fig. 5a and b display the CSD in volume and in cumulative volume-based distribution, respectively, of the initial bCC, DM-bCC, and WM-bCC samples. The cumulative volume distribution plot allows for visual observation of the percentiles (D) of the particle's population, which represent the percentages of cumulative volume undersize distribution, *i.e.*, the proportion of the total volume corresponding to particles smaller than a given size. It is shown a reduction of D_{50} (median of the distribution) of the mechanochemically treated samples from 17.3 μm to 13.2 μm for DM-bCC and to 8.7 μm for the WM-bCC sample. Considering the size of the isolated particles observed by SEM of samples DM-bCC and WM-bCC after disassembling the bigger bCC plaques (Fig. 3a–c), it is evident that D_{50} is greatly affected by particles aggregation. When transforming the starting materials to Ap (Fig. 5c and d), the D_{50} slightly increased from 337 nm for the 160 °C-Ap sample to 392 nm for 80 °C-DM-Ap, and to 420 nm for the 40 °C-WM-Ap. The percentile D_{10}, which is closer to the size of the individual particles, also increases from 219 to 222 and 239 nm. Comparing to the particle size observed by SEM, it is evident that even D_{10} is affected by particle aggregation. For these samples, the D_{90}, fully affected by aggregation, increases from 557 nm for the 160 °C-Ap to 891 nm for the 40 °C-WM-Ap and to 1548 nm for the 80 °C-DM-Ap sample. In any case, the size of aggregates is around the micron.

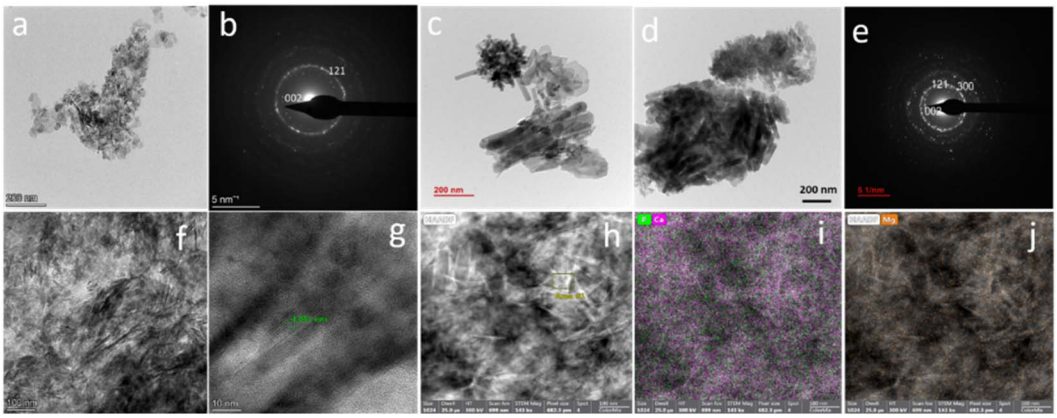

Fig. 4 TEM micrographs of samples 80 °C-DM-Ap (a) and 40 °C-WM-Ap (c) and (d) at different magnifications, and the corresponding indexed SAED patterns (b) and (e). HRTEM images of the 80 °C-DM-Ap sample (f) and (g), with image (g) displaying the lattice fringes of the Ap (100) plane with a d-spacing of 0.81 nm, are shown in the second row. For the 80 °C-DM-Ap sample, the BF HAADF-STEM image (h) and EDX element mappings of Ca, P (i), and Mg (j) are further included.

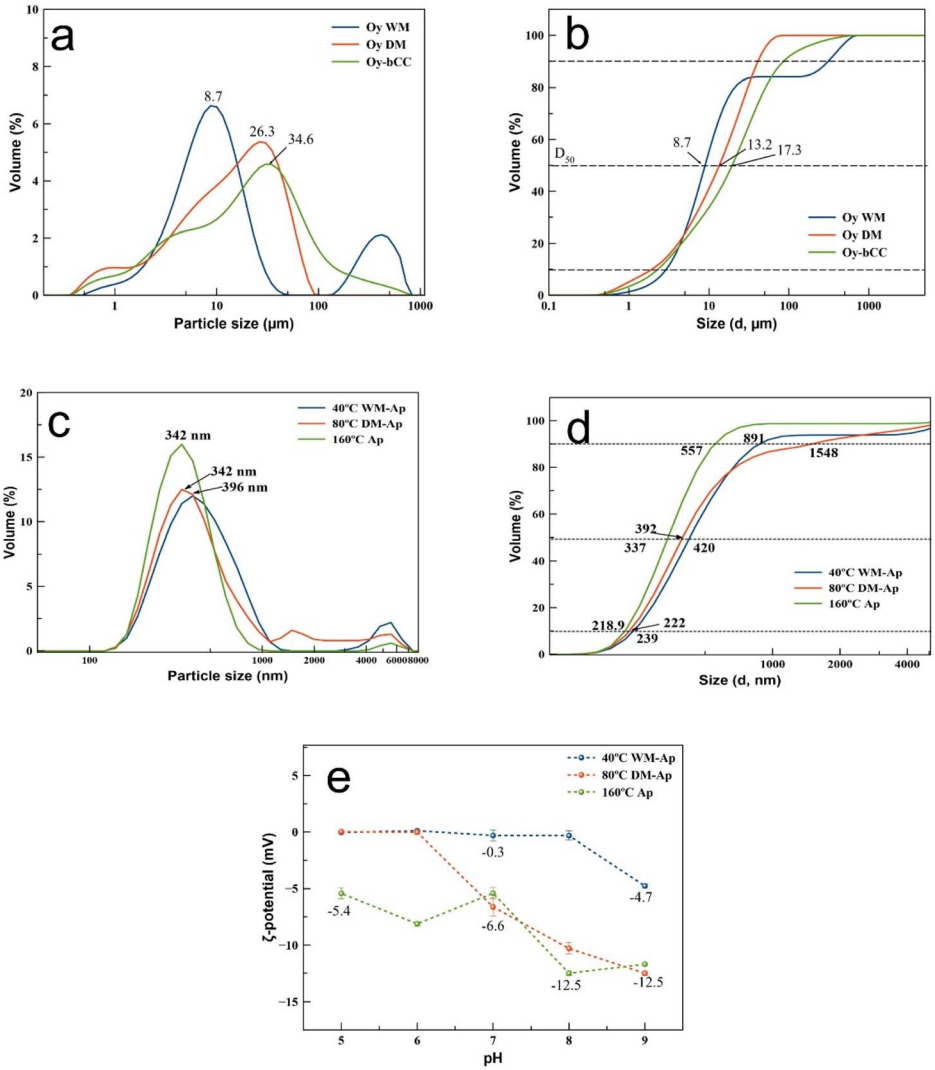

Fig. 5 Crystal size distribution and cumulative volume-based distribution of the starting $CaCO_3$ materials bCC, DM-bCC, and WM-bCC (a) and (b), and of the corresponding apatites 160 °C-Ap, 80 °C-DM-Ap and 40 °C-WM-Ap (c) and (d). ζ-Potential *versus* pH measurements of samples 160 °C-Ap, 80 °C-DM-Ap and 40 °C-WM-Ap (e).

It is also observed that the ζ-potential of the Ap samples (Fig. 5e) decreases in the pH range from 6 to 9. The minimum values are −12.5 mV for the 160 °C-Ap and 80 °C-DM-Ap samples, while values for the 40 °C-WM-Ap sample range from −0.3 mV to −4.7 mV. These low ζ-potentials inform a lack of stability of the aqueous suspensions containing these particles, particularly for the 40 °C-WM-Ap sample. The notable trend to aggregation of these particles suggests potential applications as a filler implantable material rather than as drug delivery nanocarriers. To enhance particle repulsion, and then, improve the stability of the suspensions, necessary for using nanoparticles as nanocarriers in drug delivery, higher ζ-potential values of <−25 or −30 mV would be required.[51]

3.4. Biological properties of mechanochemically treated bCCs and derived apatite particles

MTT-based cell viability tests were conducted on MS1 endothelial cells and on murine mesenchymal stem cells (m17.1 ASC) to assess the cytotoxic effects of the particles over a range of concentrations (0.1, 1, 10, and 100 μg mL^{-1}). As reported in Fig. 6, in both cell lines, untreated controls (CTRL-) maintained high viability, serving as a baseline for comparison. The viability levels of bCC, DM-bCC, and WM-bCC were almost identical to those of controls at all concentrations, indicating minimal cytotoxicity. These results indicate that the impact of the mechanochemical treatment on the cytotoxicity is negligible, and the biocompatibility of these compounds is preserved, aligning with previous findings on the low toxicity of the biogenic $CaCO_3$.[30] Furthermore, for the samples 160 °C Ap, 80 °C DM-Ap, and 40 °C WM-Ap, the cell viability was consistently greater than 80% in every treatment, surpassing the 70% threshold recommended by ISO 10993-5:2009.[52] However, a slight concentration-dependent reduction in cell viability, particularly evident at 100 μg mL^{-1}, is observed. This effect was more pronounced in the more fragile m17.1 ASC cells (Fig. 6b). Both findings are in agreement with previous results on the

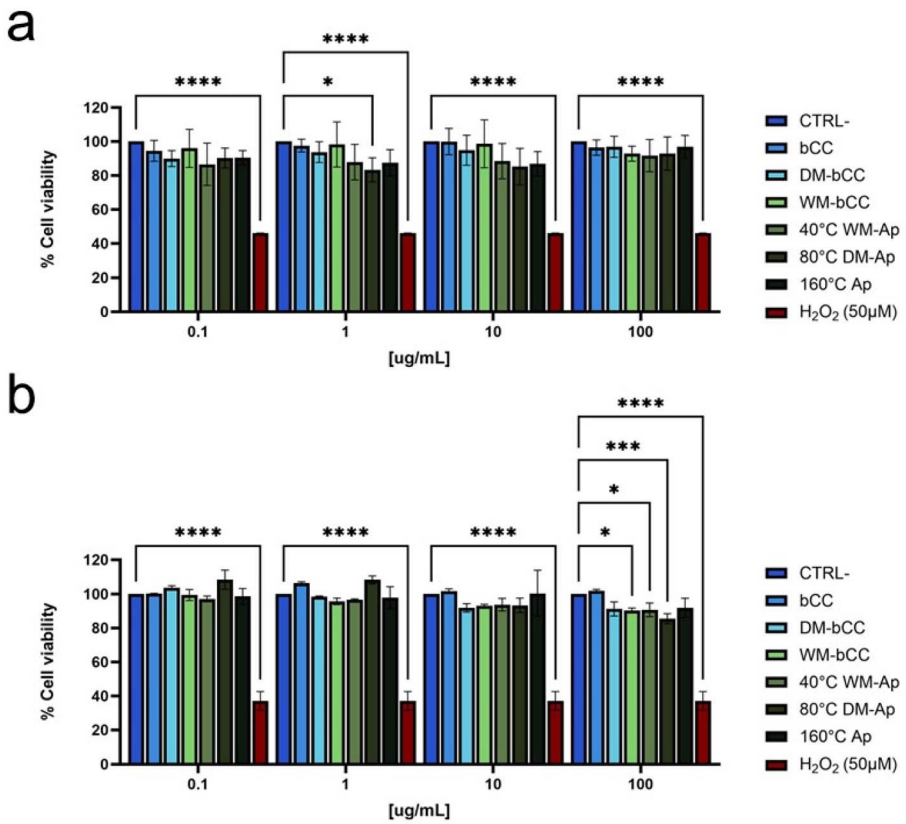

Fig. 6 MS1 (a) and m17.1 ASC cells (b) were treated for 72 hours with different (bCC, DM-bCC, WM-bCC, 40 °C WM-Ap, 80 °C WM-Ap and 160 °C WM-Ap) nanoparticles concentrations (0.1, 1, 10, and 100 μg mL^{-1}), and cell viability was evaluated using the MTT test. Histograms show the mean ± standard deviation of three independent tests. H_2O_2 (50 μM) was used as internal control of cell death while untreated cells were considered at 100% cell viability. Statistical analyses were carried out using one-way ANOVA with Dunnett's multiple comparisons test; significance is indicated as follows: *$p < 0.05$, **$p < 0.01$, ***$p < 0.001$, ****$p < 0.0001$.

cytocompatibility of apatitic samples.[53,54] As expected, the single treatment of 50 μM H_2O_2 had an impact on both cell lines, lowering their viability to less than 50%. These findings thus demonstrate the great cytocompatibility of both mechanochemically treated bCC samples and derived Ap NPs samples. The results not only reinforce the safety profile of mechanochemically treated bCC and its apatitic derivatives but also support their potential application in biomedical scenarios where cellular compatibility is paramount. Indeed, Ap crystals can be commonly used as fillers in composites with various polymers and crosslinkers to improve the mechanical properties and overall effectiveness of 3D implantable scaffolds,[55] or as nano-HAp based porous scaffolds prepared by selective laser sintering (SLS) or calcination,[56,57] as ceramics obtained by spark plasma sintering (SPS),[58] or as delivery platforms of drugs or bioactive molecules such as bone-morphogenetic protein-2 (BMP-2), vancomycin, calcitriol, dexamethasone, and cisplatin for promoting bone regeneration.[59] Their application in bone tissue engineering offers promising outcomes for the restoration of skeletal deficiencies, including orthopaedic conditions, chronic osteomyelitis, and periodontal bone defects, by effectively replacing damaged or lost bone structures.[60–62] Nevertheless, it is important to emphasize that further *in vitro* studies are necessary to investigate the interactions of the NPs with different cell types and biological microenvironments. Such investigations will be crucial for tailoring these materials to specific biomedical applications, ensuring their safety, efficacy, and functional performance under conditions that closely mimic the intended biological use.

4. Conclusions

The coupling of mechanochemical treatments of bCC to the one-pot hydrothermal synthesis to obtain Ap NPs has led to a significant reduction of T_{min}. The DM mechanochemical treatment (1 h) produced a decrease in crystallite size of the calcitic bCC particles from 92 to 14 nm. Consequently, when submitted bCC-DM to hydrothermal conversion the T_{min} reduced from 160 °C to 80 °C. The extended WM treatment (18 h), however, induced polymorphism and amorphization of the bCC, yielding a mixture of calcite, aragonite and ACC, with crystallites size of 7 nm for calcite and 13.7 nm for aragonite. In this case T_{min} reduced to 40 °C. The transformation of bCC-DM into Ap at 80 °C was faster than that of bCC-WM at 40 °C, achieving 98% transformation *versus* 82% after 4 days. Nevertheless, in both cases the complete transformation took 7 days. The obtained Ap crystals display, in general, a great tendency to aggregate in physiological conditions, particularly the 40 °C-

WM-Ap sample, as revealed by the analysis of the CSD and the ζ-potential *versus* pH measurements. The mechanochemically treated bCCs and the derived Ap NPs were all cytocompatible on MS1 endothelial cells and on murine mesenchymal stem cells (m17.1 ASC) according to ISO 10993-5:2009. A slight concentration-dependent reduction in cell viability was observed at the highest concentration (100 μg mL^{-1}), and particularly on m17.1 ASC cells. The great tendency for Ap crystals to aggregate, linked to the biocompatibility of the NPs, suggests applications as a filler implantable material (after sintering of the Ap NPs by SLS or SPS) rather than as drug/biomolecule delivery nanocarriers, for these particles. Compared with previous hydrothermal approaches, the decrease of T_{min} to 80 °C or 40 °C, paves the way to scale up the process using already established glass reactor technology in the industry, thereby making unnecessary the use of big and expensive hydrothermal autoclaves. This is a determinant incentive in favor of the proposed mechanochemical treatments coupled to the one-pot hydrothermal method, to valorize the oyster shells.

Author contributions

Conceptualization, J. G.-M., G. F., A. F.; investigation, C. T., F. O., A. D., A. F., R. F. P.; methodology, J. G.-M., G. F., A. F., F. O.; supervision, J. G.-M., F. O.; writing—original draft preparation, J. G.-M., F. O.; writing—review and editing, J. G.-M., F. O., A. F., G. F.; funding acquisition, J. G.-M., F. O., A. F. All authors have read and agreed to the published version of the manuscript.

Conflicts of interest

The authors declare no competing interests.

Data availability

The authors declare that the data supporting this study's findings are available within the paper and its supplementary information (SI). Should any raw data files be needed in another format, they are available from the corresponding author upon reasonable request. Supplementary information: Fig. S1 – XRD patterns showing the evolution of the transformation of (a) dry-milled bCC samples into calcium phosphates at temperatures between 25 °C and 120 °C and (b) of the wet-milled bCC samples into calcium phosphates within the temperature range from 25 °C to 80 °C; Fig. S2 – XRD patterns showing the evolution of the transformation of (a) dry-milled bCC samples at 80 °C and (b) of the wet-milled bCC samples at 40 °C into calcium phosphates in the time range from 6 h to 7 days. See DOI: https://doi.org/10.1039/d5su00830a.

Acknowledgements

This publication is part of the Project GBRMat ref. 2023-151538NB-100, funded by Spanish MCIU/AEI/10.13039/501100011033 and "FEDER una manera de hacer Europa", UE. FO acknowledges the project ARCHER that has received funding from the MUR–M4C2 I1.2 of PNRR with ID project no. MSCA_0000008. AF was supported by PNRR MUR code CN00000041, Program "National Center for Gene Therapy and Drugs based on RNA Technology": ALLEVIATE "Safe and long-term *in vivo* tolerogenic expression of FVIII by LV targeting hepatic endothelial cells 30/07, and PRIN-PNRR, Code: 2022CAWRK5: "TolerEight: Cellular and molecular mechanisms governing immune tolerance to protein and gene replacement therapy in hemophilia" 28/02.

References

1 Hydroxyapatite Market Size & Share, *Hydroxyapatite Market Size & Share | Industry Report, 2030; Grand View Research Report ID:GVR-4-68040-534-4*, 2025, https://www.grandviewresearch.com/industry-analysis/hydroxyapatite-market-report.
2 N. K. Nga, N. T. T. Chau and P. H. Viet, *Colloids Surf., B*, 2018, **172**, 769–778.
3 S. Scialla, F. Carella, M. Dapporto, S. Sprio, A. Piancastelli, B. Palazzo, A. Adamiano, L. Degli Esposti, M. Iafisco and C. Piccirillo, *Mar. Drugs*, 2020, **18**, 309.
4 A. Pal, S. Maity, S. Chabri, S. Bera, A. R. Chowdhury, M. Das and A. Sinha, *Biomedical Physics & Engineering Express*, 2017, **3**, 015010.
5 S. H. Saharudin, J. H. Shariffuddin, N. I. A. A. Nordin and A. Ismail, *Mater. Today: Proc.*, 2019, **19**, 1208–1215.
6 S. Rujitanapanich, P. Kumpapan and P. Wanjanoi, *Energy Procedia*, 2014, **56**, 112–117.
7 A. Shavandi, A. E.-D. A. Bekhit, A. Ali and Z. Sun, *Mater. Chem. Phys.*, 2015, **149**, 607–616.
8 Y. Xu, D. Wang, L. Yang and H. Tang, *Mater. Charact.*, 2001, **47**, 83–87.
9 H. Ivankovic, E. Tkalcec, S. Orlic, G. Gallego Ferrer and Z. Schauperl, *J. Mater. Sci.: Mater. Med.*, 2010, **21**, 2711–2722.
10 D. Summa, M. Lanzoni, G. Castaldelli, E. A. Fano and E. Tamburini, *Resources*, 2022, **11**, 48.
11 Y. Hou, A. Shavandi, A. Carne, A. A. Bekhit, T. B. Ng, R. C. F. Cheung and A. E. A. Bekhit, *Crit. Rev. Environ. Sci. Technol.*, 2016, **46**, 1047–1116.
12 N. Yan and X. Chen, *Nature*, 2015, **524**, 155–157.
13 K. H. Mo, U. J. Alengaram, M. Z. Jumaat, S. C. Lee, W. I. Goh and C. W. Yuen, *Constr. Build. Mater.*, 2018, **162**, 751–764.
14 D. Suteu, D. Bilba, M. Aflori, F. Doroftei, G. Lisa, M. Badeanu and T. Malutan, *Clean: Soil, Air, Water*, 2012, **40**, 198–205.
15 P. Morseletto, *Resour., Conserv. Recycl.*, 2020, **153**, 104553.
16 M. Florin, M. A. Cătălina, S. E. George, M. Andreea, M. Marian, V. S. Ioan and I. Antoniac, *Bioceramics and biocomposites: from research to clinical practice*, 2019, pp. 87–122.
17 S. Santhosh and S. Balasivanandha Prabu, *Mater. Lett.*, 2013, **97**, 121–124.
18 B. N. Alhussary, G. A. Taqa and A. A. A. Taqa, *Journal of Applied Veterinary Sciences*, 2020, **5**, 25–32.
19 D. L. Goloshchapov, A. S. Lenshin, D. V. Savchenko and P. V. Seredin, *Results Phys.*, 2019, **13**, 102158.

20 D. F. Fitriyana, R. Ismail, Y. I. Santosa, S. Nugroho, A. J. Hakim and M. S. Al Mulqi, in *2019 International Biomedical Instrumentation and Technology Conference (IBITeC)*, IEEE, 2019, vol. 1, pp. 7–11.
21 P. Baláž, M. Achimovičová, M. Baláž, P. Billik, Z. Cherkezova-Zheleva, J. M. Criado, F. Delogu, E. Dutková, E. Gaffet and F. J. Gotor, *Chem. Soc. Rev.*, 2013, **42**, 7571–7637.
22 T. Tsuzuki, *Commun. Chem.*, 2021, **4**, 143.
23 Z. Shalabayev, M. Baláž, N. Khan, Y. Nurlan, A. Augustyniak, N. Daneu, B. Tatykayev, E. Dutková, G. Burashev and M. Casas-Luna, *Nanomaterials*, 2022, **12**, 1250.
24 M. Nuruzzaman, Y. Liu, M. M. Rahman, S. O. Nasif and R. Naidu, *Appl. Nano*, 2025, **6**, 8.
25 T. Mandal, B. K. Mishra, A. Garg and D. Chaira, *Powder Technol.*, 2014, **253**, 650–656.
26 F. Cestari, G. Chemello, A. Galotta and V. M. Sglavo, *Ceram. Int.*, 2020, **46**, 23526–23533.
27 F. Cestari, F. Agostinacchio, A. Galotta, G. Chemello, A. Motta and V. M. Sglavo, *Nanomaterials*, 2021, **11**, 264.
28 A. Galotta, F. Agostinacchio, A. Motta, S. Dire and V. M. Sglavo, *J. Eur. Ceram. Soc.*, 2023, **43**, 639–647.
29 A. F. Lemos, J. H. G. Rocha, S. S. F. Quaresma, S. Kannan, F. N. Oktar, S. Agathopoulos and J. M. F. Ferreira, *J. Eur. Ceram. Soc.*, 2006, **26**, 3639–3646.
30 R. Fernández-Penas, C. Verdugo-Escamilla, C. Triunfo, S. Gärtner, A. D'Urso, F. Oltolina, A. Follenzi, G. Maoloni, H. Cölfen and G. Falini, *J. Mater. Chem. B*, 2023, **11**, 7766–7777.
31 S. M. Cano-Plá, F. Oltolina, F. J. Acebedo-Martínez, R. Fernández-Penas, C. Verdugo-Escamilla, C. Triunfo, P. E. Di Simone, C. Borsotti, A. Follenzi and G. Maoloni, *Sci. Rep.*, 2025, **15**, 10893.
32 T. Wen, Y. Zhao, T. Zhang, B. Xiong, H. Hu, Q. Zhang and S. Song, *Chemosphere*, 2020, **246**, 125842.
33 C. Marchini, C. Triunfo, N. Greggio, S. Fermani, D. Montroni, A. Migliori, A. Gradone, S. Goffredo, G. Maoloni and J. Gómez Morales, *Cryst. Growth Des.*, 2023, **24**, 657–668.
34 A. Zamperone, S. Pietronave, S. Merlin, D. Colangelo, G. Ranaldo, E. Medico, F. Di Scipio, G. N. Berta, A. Follenzi and M. Prat, *Stem Cells Dev.*, 2013, **22**, 2873–2884.
35 J. M. Delgado-López, M. Iafisco, I. Rodríguez, A. Tampieri, M. Prat and J. Gómez-Morales, *Acta Biomater.*, 2012, **8**, 3491–3499.
36 L. Wang and G. H. Nancollas, *Chem. Rev.*, 2008, **108**, 4628–4669.
37 H. McDowell, T. M. Gregory and W. E. Brown, *J. Res. Natl. Bur. Stand., Sect. A*, 1977, **81**, 273.
38 M. T. Fulmer and P. W. Brown, *J. Mater. Res.*, 1993, **8**, 1687–1696.
39 L. Niel Plummer and E. Busenberg, *Geochim. Cosmochim. Acta*, 1982, **46**, 1011–1040.
40 M. Percival, *Appl. Nutr. Sci. Rep.*, 1999, **5**(4), 1–6.
41 E. Landi, G. Logroscino, L. Proietti, A. Tampieri, M. Sandri and S. Sprio, *J. Mater. Sci.: Mater. Med.*, 2008, **19**, 239–247.
42 F. Oltolina, L. Gregoletto, D. Colangelo, J. Gomez-Morales, J. M. Delgado-López and M. Prat, *Langmuir*, 2015, **31**, 1766–1775.
43 A. Barroug and M. J. Glimcher, *J. Orthop. Res.*, 2002, **20**, 274–280.
44 V. Uskoković and T. A. Desai, *J. Biomed. Mater. Res., Part A*, 2013, **101**, 1416–1426.
45 T. Ikoma, M. Tagaya, N. Hanagata, T. Yoshioka, D. Chakarov, B. Kasemo and J. Tanaka, *J. Am. Ceram. Soc.*, 2009, **92**, 1125–1128.
46 P. N. Kumta, C. Sfeir, D.-H. Lee, D. Olton and D. Choi, *Acta Biomater.*, 2005, **1**, 65–83.
47 S. Y. Alhaji, E. H. Chowdhury, R. Rosli, F. Hassan and S. Abdullah, *BioMed Res. Int.*, 2014, **2014**, 646787.
48 S. M. Cano Plá, A. D'urso, J. F. Fernández-Sánchez, D. Colangelo, D. Choquesillo-Lazarte, R. Ferracini, M. Bosetti, M. Prat and J. Gómez-Morales, *Nanomaterials*, 2022, **12**, 562.
49 Z. Wang, T. Han, H. Zhu, J. Tang, Y. Guo, Y. Jin, Y. Wang, G. Chen, N. Gu and C. Wang, *Nanoscale Res. Lett.*, 2021, **16**, 67.
50 T. Riley, T. Govender, S. Stolnik, C. D. Xiong, M. C. Garnett, L. Illum and S. S. Davis, *Colloids Surf., B*, 1999, **16**, 147–159.
51 K. Öztürk, M. Kaplan and S. Çalış, *Int. J. Pharm.*, 2024, **666**, 124799.
52 International Standard, ISO 10993-5:2009(en), *Biological evaluation of medical devices—Part 5: Tests for in vitro cytotoxicity*, International Organization for Standardization, Geneva, Switzerland, 2009, vol. 10, DOI: 10.2345/9781570203558.
53 F. J. Martínez-Casado, M. Iafisco, J. M. Delgado-López, C. Martínez-Benito, C. Ruiz-Perez, D. Colangelo, F. Oltolina, M. Prat and J. Gomez-Morales, *Cryst. Growth Des.*, 2016, **16**, 145–153.
54 P. Puentedura-Navarro, R. Fernández-Penas, F. J. Acebedo-Martínez, C. Triunfo, J. F. Fernández-Sánchez, A. Follenzi, F. Oltolina, G. Falini and J. Gómez-Morales, *CrystEngComm*, 2025, **27**, 1078–1089.
55 S. Soleymani and S. M. Naghib, *Heliyon*, 2023, **9**(9), e19363.
56 P. Feng, M. Niu, C. Gao, S. Peng and C. Shuai, *Sci. Rep.*, 2014, **4**, 5599.
57 F. Scalera, F. Gervaso, K. P. Sanosh, A. Sannino and A. Licciulli, *Ceram. Int.*, 2013, **39**, 4839–4846.
58 D. Grossin, S. Rollin-Martinet, C. Estournès, F. Rossignol, E. Champion, C. Combes, C. Rey, C. Geoffroy and C. Drouet, *Acta Biomater.*, 2010, **6**, 577–585.
59 A. S. Mohd Zaffarin, S.-F. Ng, M. H. Ng, H. Hassan and E. Alias, *Nanomaterials*, 2021, **11**, 2569.
60 F. Fendi, B. Abdullah, S. Suryani, A. N. Usman and D. Tahir, *Bone*, 2024, **183**, 117075.
61 J. Wang, Q. Zhang, H. Wang, C. Liu, L. Jiang, W. Liu, Y. Wu, Y. Wang, H. Yan and J. Lin, *Biomaterials*, 2025, **314**, 122899.
62 R. Izzetti, S. Gennai, M. Nisi, F. Gulia, M. Miceli and M. R. Giuca, *Appl. Sci.*, 2022, **12**, 10762.